The Influence of Rotor/Wing Aerodynamic Interaction of Compound Helicopter in Forward Flights on Wing-body

Yusuke Hamamoto, Graduate School of Kanazawa Institute of Technology (Japan)
Takeshi Akasaka, Kanazawa Institute of Technology (Japan)
Yasutada Tanabe, Japan Aerospace Exploration Agency (Japan)
Hideaki Sugawara, Japan Aerospace Exploration Agency (Japan)

Abstract

This paper investigates the influence on aerodynamic characteristics of a winged-body of a rotor/winged-body configuration due to changes of the advance ratio through numerical simulations. A winged compound helicopter has a single main rotor and a fixed-wing located under the rotor. Due to the configuration, an aerodynamic interaction occurs between the rotor and the wing. In high advance ratio flight, the aerodynamic interaction produces asymmetrical aerodynamic characteristics on the left and right sides of the wing. This phenomenon is dependent on the rotor flow field and is presumed to be changed by the advance ratio. Therefore, in this paper, the asymmetrical aerodynamic characteristics of the wing were investigated for advance ratio from 0.1 to 0.7. A computational model is constituted by the UH-60A main rotor only the blades and the winged-body. The winged-body combines a rectangle wing and a fuselage designed by JAXA. The wing has span length that of 0.7 times of the rotor diameter and an aspect ratio of 10. The rotor speed was scheduled to decrease along with increasing flight speed. The combination for this simulation was selected from the schedule in order to correspond to the advance ratio from 0.1 to 0.7. As a result, the lift coefficient, drag coefficient and lift-to-drag ratio of both sides on the wing of the rotor/winged-body configuration becomes closer to that of the isolated winged-body as the advance ratio increases, but that of the right side, witch is under the advancing side of the rotor, remains different to that of the isolated winged-body. The influences on the lift and drag coefficient are stronger at the root than the tip on the wing, at the right side more than the left side and at low advance ratio than at high advance ratio.

NOTATION

Symbol	Definition
a_∞	Sound of speed
b	Wing span
c_w	Wing chord
c_d	Sectional drag coefficient, $d/(1/2\rho_\infty V_\infty^2 c_w)$
c_l	Sectional lift coefficient, $l/(1/2\rho_\infty V_\infty^2 c_w)$
C_{LR}	Lift coefficient of rotor, $L_R/(\rho_\infty \pi R^2 (R\Omega)^2)$
C_{LT}	Lift coefficient of total of rotor and winged-body, $L_T/(\rho \pi R^2 (R\Omega)^2)$
C_{LW}	Lift coefficient of total of winged-body, $L_W/(\rho \pi R^2 (R\Omega)^2)$
C_{p_∞}	Pressure coefficient, $(p - p_\infty)/(1/2\rho_\infty V_\infty^2)$
d	Sectional drag
D	Drag
l	Sectional Lift
L	Lift
L_R	Lift of rotor
L_T	Lift of total of rotor and winged-body
L_W	Lift of winged-body
M_∞	Uniform flow Mach number, V_∞/a_∞
R	Rotor radius
S_w	Reference area of winged-body
u	Flow velocity in the direction of the uniform flow (nondimensionalized by the speed of sound)
V_∞	Uniform flow velocity
y	Lateral location (positive to right)
y/R	Lateral location nondimensionalized by rotor radius
ΔC_{DW}	Increment of drag coefficient of winged-body, $(D_{RWI} - D_{Isolated})/(1/2\rho_\infty V_\infty^2 S_w)$
ΔC_{LW}	Increment of lift coefficient of winged-body, $(L_{RWI} - L_{Isolated})/(1/2\rho_\infty V_\infty^2 S_w)$
Δu	Increment of flow velocity in the direction of the uniform flow, $u - M_\infty$
μ	Advance ratio, $V_\infty/(R\Omega)$
ρ_∞	Uniform flow density
Ω	Rotor angular velocity
$()_{Isolated}$	Isolated winged-body
$()_{RWI}$	Rotor/winged-body configuration

1. Introduction

Helicopters are operated for disaster-relief activities, emergency rescues and cargo transportations because they have excellent hover and VTOL performance. These operations require the improvement of the maximum flight speed of helicopters. However, as the flight speed increases, the Mach number on blades at the advancing side becomes closer to the speed of sound and the blade pitch angle becomes closer to the limit due to a reverse flow region at the retreating side. As a solution, tilt rotors and compound helicopters are suggested [1]. Helicopters tilt the tip path plane of the main rotor to generate the propulsion, while compound helicopters are installed propellers or jet engines to decrease the blade load of the main rotor. The compound helicopters are mainly classified into two types according to the configuration [1]. The two types are Coaxial compound helicopters like the X2 developed by Sikorsky Aircraft [2] and winged compound helicopters like the X^3 developed by Airbus Helicopters [3]. The X2 and X^3, which represent compound helicopters, were proven to improve maximum flight speed through flight tests [2, 3]. The demonstrators X2 and X^3 are the basis for the RAIDER and the RACER under development, respectively.

Winged compound helicopters with a single rotor and a fixed-wing under the main rotor has the technical issue that the rotorcraft's effective lift-to-drag ratio decreases due to the aerodynamic interaction between the main rotor and wing. Therefore, the investigation of the aerodynamic interaction is required to design winged compound helicopters with a high effective lift-to-drag ratio.

The rotor/wing aerodynamic interaction in forward flight is investigated by various researches. Leishman conducted wind tunnel tests configurated with a rotor, fuselage and one wing at advance ratios from 0.05 to 0.25 [4]. Sugawara simulated same configuration through CFD (Computational Fluid Dynamics), and verified the CFD results with wind tunnel tests [5]. Moreover, Sugawara performed numerical simulations configurated with a rotor and rectangle wing without airframe at advance ratios of 0.7 and 0.8 [5]. Wentrup performed CFD on a configuration with an actuator disk and the RACER airframe [6], and Frey performed CFD on the full RACER configuration [7]. Sugawara [8], Hamamoto [9] and Tanabe [10] performed numerical simulations on a rotor and winged-body configuration. In particular, Tanabe conducted CFD and wind tunnel tests at an advance ratio of 0.5, and verified the results of CFD and wind tunnel tests [10]. Several previous researches [5-8,10] indicated that the aerodynamic interaction causes asymmetric aerodynamic characteristics on the wing under the advancing and retreating side of the main rotor in a high advance ratio. The asymmetric effect of the aerodynamic interaction on the wing is presumed to become strong as the advance ratio increases.

The previous work on Ref. 9 addressed the influence of the advance ratio on the basic aerodynamic performance of compound helicopter with the rotor/winged-body aerodynamic interaction using numerical simulations. Therefore, this paper extends Ref. 9 by focusing on the asymmetric aerodynamic characteristics of the wing, and investigates the influence of the advance ratio on the aerodynamic characteristics of the rotor/winged-body in the rotor/winged-body aerodynamic interaction over the advance ratios from 0.1 to 0.7.

2. Computational Model

The main rotor blade of the computational model is that of UH-60A designed by Sikorsky. This rotor has a radius of 8.18 m, an equivalent blade twist of -16 deg and four blades. The direction of rotation is counter-clockwise. The detailed specifications are described in Ref. 11,12.

Fig. 1 shows the winged-body model. The fuselage shape is the same shape as in Ref. 8. The wing of the model has incidence angle of 4.2 deg and the wing span is 0.7 times the rotor diameter. The airfoil is NACA4415 and the planform is rectangle. The wing is located under the rotor, at a distance of 0.235 times the rotor radius from center of the rotor. The reference area of the winged-body is 13.115 m^2, as indicated by the shaded area. The right side of the wing is located under the advancing side of the rotor, the left side is located under the retreating side.

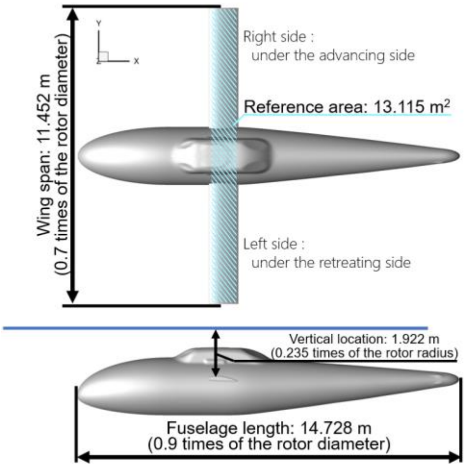

Fig. 1 Winged-body model overview.

3. Numerical methods

The rFlow3D [13] CFD solver for rotorcrafts developed by JAXA was used in this paper. The rFlow3D adopts a moving overlapped grid method. The rotor blades are covered with the moving overlapped grids, and a background grid overlaps the rotor blades grids. The governing equations are the three-dimensional compressible Navier-Stokes equations discretized with the finite-volume method. The time integration used for the background orthogonal grids are the four-stages Runge-Kutta. The blades and the winged-body used the implicit method which adopts the dual-time-stepping method and the LU-SGS method. The numerical flux is obtained by using mSLAU (modified SLAU for the moving grid method). The reconstruction adopts the Fourth-order Compact MUSCL TVD scheme. The viscous flux adopts a second-order centered difference method. The turbulence model is adopted Menter k-ω SST 2003 model.

Fig. 2 shows the computational grid. The resolution of the inner background grid is 15 % of the blade chord length of the rotor. The resolution of the outer background grid overlapping the inner background grid is two times that of the inner background grid and the no overlapping area becomes coarse with increasing distance. The minimum grid hight on the surface of the blades and the winged-body are less than $y^+=1$. The same grids are utilized for all calculation in this paper, although the computational condition varies the uniform velocity and the rotational speed of the rotor.

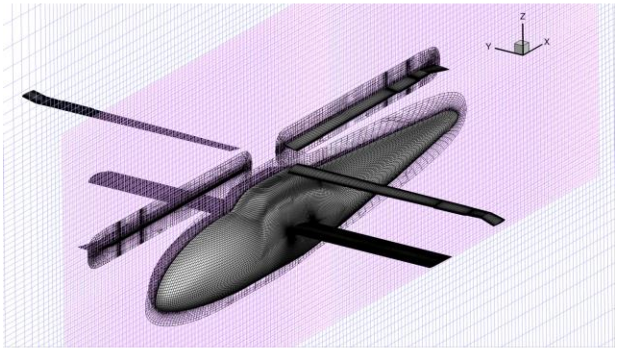

Fig. 2 Overview of the overlapped CFD grids

4. Computational conditions

The shaft angle of the main rotor was 0 deg. The blade flap, lead-lag motion, and the blade elastic deformation were not considered. The gross weight was 97860.8 N [14] which is the maximum takeoff gross weight of UH-60A. Fig. 3 shows the rotor speed schedule based on the rotor speed in hover. The 100 %RPM was 258 RPM [14], which refers to the rotor speed of UH-60A in hover. The rotor speed decreases as the advance ratio increases. The minimum rotational speed was 75 %RPM at an advance ratio above 0.65. The advance ratio was changed from 0.1 to 0.7, and numerical simulations were carried out on the eight cases of flight conditions shown in Fig. 3. The uniform flow Mach number was varied from 0.065 to 0.34 along with the advance ratio.

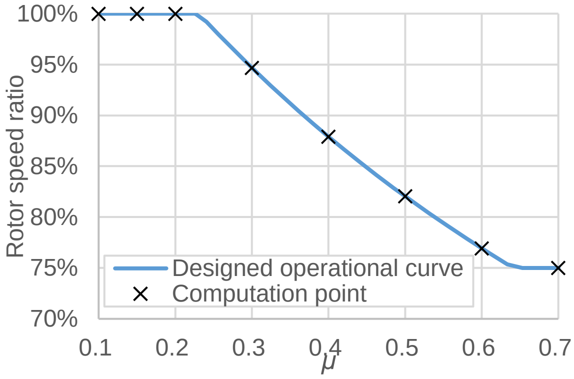

Fig. 3 Rotor speed schedule

Fig. 4 shows the computational configurations which are the rotor/winged-body configuration and the isolated winged-body. Table 1 shows the trim condition of each configurations. The configuration in Fig. 4(a) matches the gross weight with the total lift of the rotor and winged-body. The rolling moment and pitching moment of rotor is 0. The Fig. 4(b) is the isolated winged-body without the rotor.

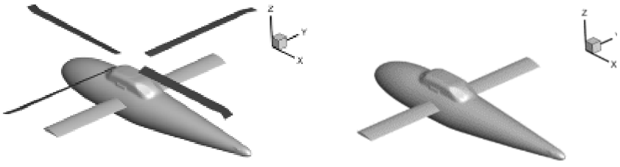
(a) Rotor/winged-body configuration (b) Isolated winged-body

Fig. 4 Computational configurations

Table 1 Trim conditions

Configuration	Trim condition	
	Lift	Moment
Rotor/winged-body config.	Total lift of rotor and wined-body = Gross weight	*Mx*=*My*=0 at rotor
Isolated winged-body	None	None

5. Results and Discussions

Fig. 5 shows the lift share of the rotor and the winged-body on the rotor/winged-body configuration. The lift share is the ratio of the lift coefficient of the rotor or the winged-body to the total lift coefficient. The lift share of the winged-body is larger than that of the rotor at the advance ratio above 0.6. The lift share of the winged-body becomes negative at advance ratios of 0.1 and 0.15 due to the rotor/winged-body aerodynamic interaction.

Fig. 6 shows the flow field around the rotor and winged-body. The wake of the rotor impinges the wing on winged-body at advance ratio of 0.1 and passes above the wing for the advance ratios from 0.15 to 0.7.

Fig. 7 shows the stream-line around the wing and the pressure coefficient nondimensionalized by dynamic pressure based on the uniform flow velocity. As a basic trend, the wake around the wing on the rotor/winged-body configuration is more deflected in the direction of decreasing the angle of attack than that on the isolated winged-body, the stagnation point of the wing on the rotor/winged-body locates above that of the isolated winged-body. The negative pressure on the upper surface of the wing is smaller than that of the isolated winged-body. These trends become stronger at the root than the tip on the wing, at the right side than the left side and at low advance ratio than high advance ratio. At the advance ratio of 0.1, the flow separates on the right side on the rotor/winged-body. The angle of attack is negative or low at advance ratios of 0.1 and 0.15.

Fig. 8 shows the increment of the flow velocity in the direction of the uniform flow around the fuselage on the winged-body. This increment of the flow velocity is nondimensionalized by the speed of sound. The velocity on the upper side of the nose of the rotor/winged-body configuration decreases more than that of the isolated winged-body. This phenomenon is caused by the flow on the isolated winged-body flowing smoother on the upper side of the nose, but that on the rotor/winged-body configuration is decelerated by the rotor downwash. The decrement of velocity on the upper side of the nose causes the lift to decrease and the drag to increase on the fuselage.

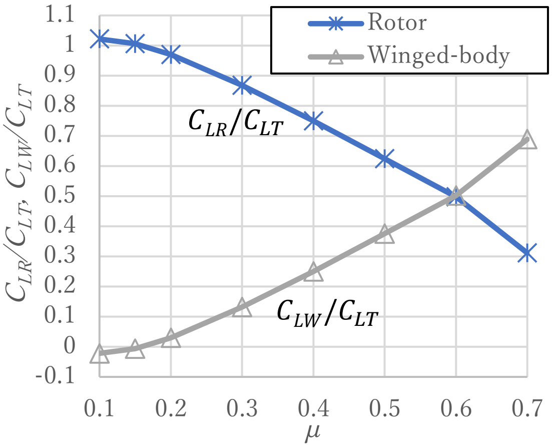

Fig. 5 The effect of rotor/winged-body aerodynamic interaction on the lift share

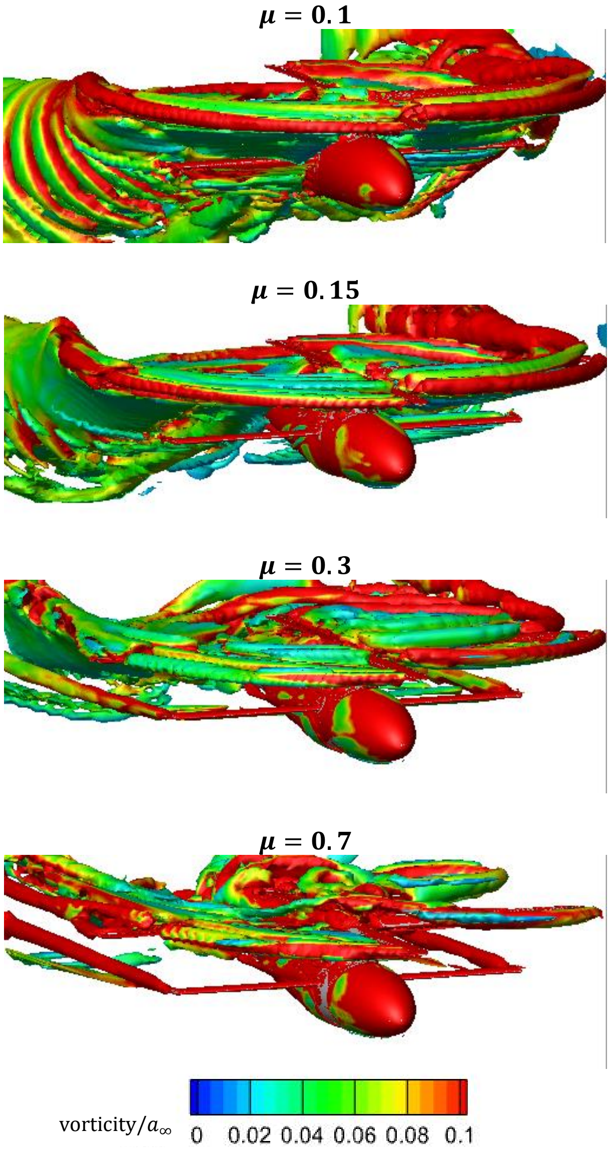

Fig. 6 Iso-surface Q-criterion around the right wing under advancing side.

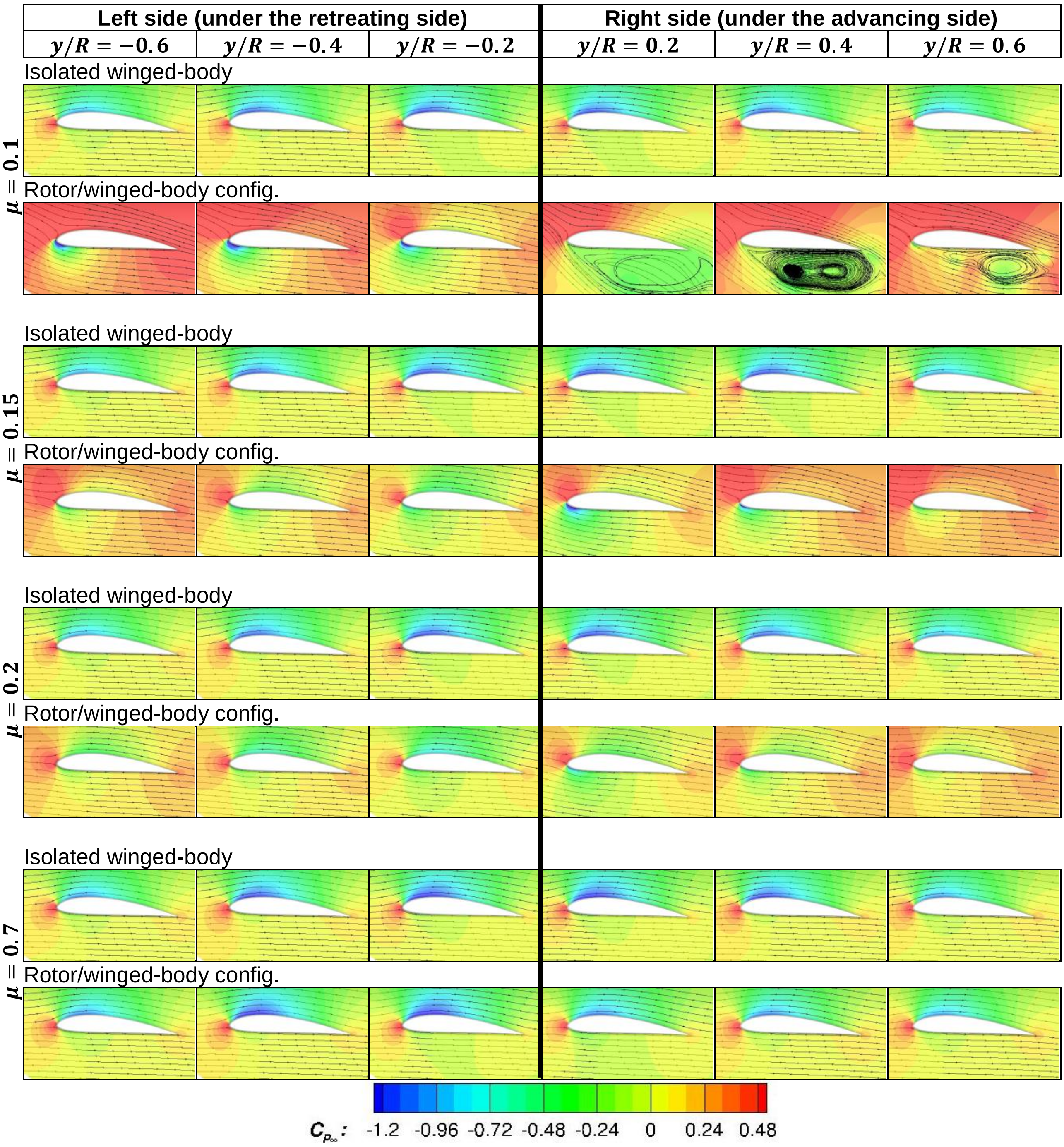

Fig. 7 Flow field of wing of winged-body. (pressure coefficient nondimensionalized by dynamic pressure based on the uniform flow velocity.)

Fig. 9 shows the distribution of the sectional lift coefficient of the wing on the winged-body. Corresponding to Fig. 7, the sectional lift coefficient on the rotor/winged-body is smaller than that on the isolated winged-body. The influence is stronger at the root than the tip of the wing, at the right side more than the left side, and at lower advance ratio than high advance ratio. The negative sectional lift coefficient generates on both sides at an advance ratio of 0.1 and on the right side at an advance ratio of 0.15. This negative sectional lift is caused by the negative angle of attack and the flow separation as shown Fig. 7. The sectional lift coefficient on left side becomes closer to that on isolated winged-body as the advance ratio increases. However, even if the advance ratio increases, the sectional lift coefficient on the right side remains different at the root side. The phenomenon is caused by the rotor downwash decreasing on the retreat side as the advance ratio increases, but the rotor downwash on the advancing side does not decrease as rapidly as on the retreating side. In particular, the large rotor downwash remains large at the root side on the advancing side because the blades used in this paper have a large blade twist.

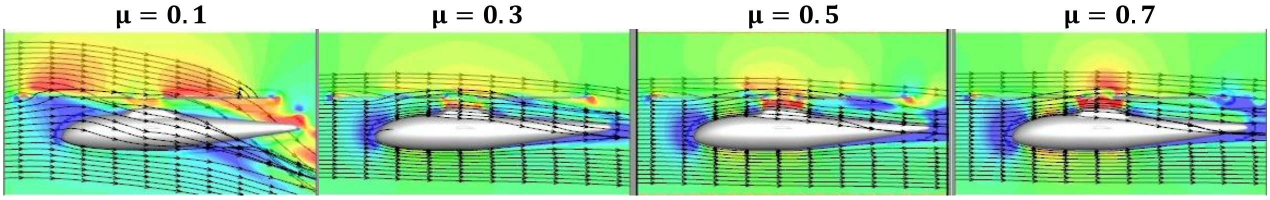

(a) Rotor/winged-body configuration

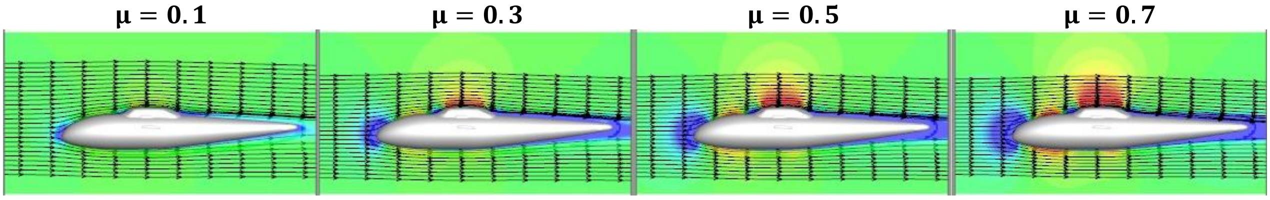

(b) Isolated winged-body configuration

Fig. 8 The increment of the flow velocity in the direction of the uniform flow around the fuselage of the winged-body. (velocity nondimensionalized by the speed of sound.)

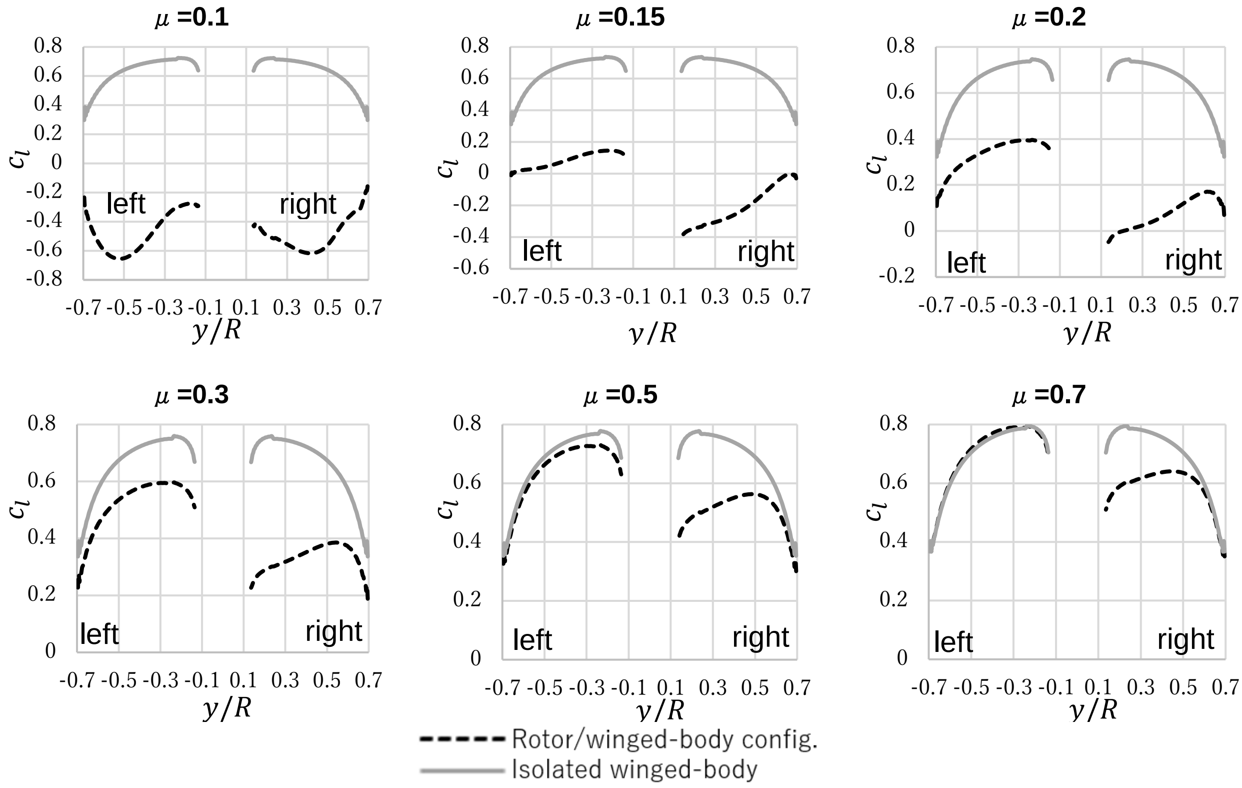

Fig. 9 The distribution of sectional lift coefficient of the wing on the winged-body.

Fig. 10 shows the distribution of the sectional drag coefficient of the wing on the winged-body. At advance ratios of 0.3 to 0.7, the sectional drag coefficient of the left side becomes closer to that on the isolated winged-body, and that of the right side remains increased at the root. At an advance ratio of

0.2, the sectional drag coefficient is larger on the left side and smaller on the right side than that on the isolated winged-body. The negative sectional drag coefficient generates on the left side at an advance ratio of 0.1 and on the right side at an advance ratio of 0.15. At an advance ratio above 0.2, the mechanism of these sectional drag increases is explained using Fig. 7, 9, 11. From Fig. 9, the sectional lift coefficient is positive at an advance ratio above 0.2. From Fig. 7, the sectional inflow angle is increased in the direction of tilting the lift vector backwards due to the rotor downwash. Therefore, as Fig. 11 shows, the backward component of tilted the lift vector increases the drag. At an advance ratio of 0.1 and 0.15, the mechanism of the negative sectional drag is explained using Fig. 7, 9, 12. From Fig. 9, the sectional lift coefficient is negative on the left side at an advance ratio of 0.1 and on the right side at an advance ratio of 0.15. From Fig. 7, the sectional inflow angle is large enough to become the negative sectional angle of attack due to the rotor downwash. As Fig. 12 shows, the large sectional inflow angle tilts the lift vector forward. Therefore, the forward component of the tilted lift vector generates the negative drag.

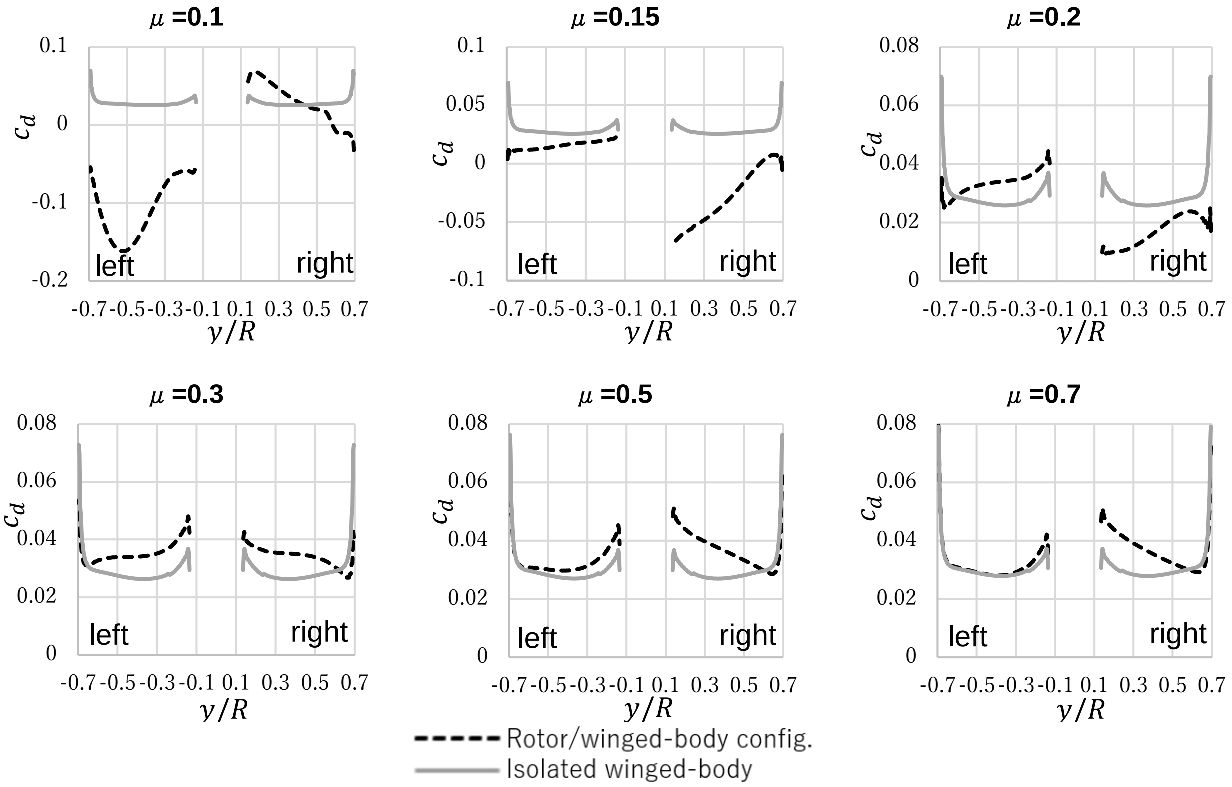

Fig. 10 The distribution of sectional drag coefficient of the wing on the winged-body.

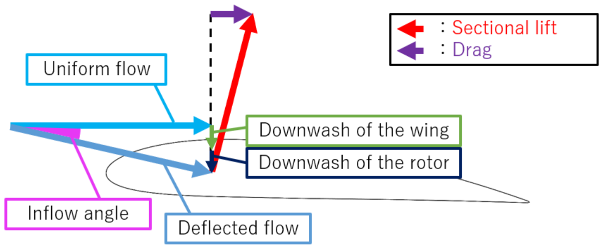

Fig. 11 The schematic of the aeromechanics which causes the increase of the drag coefficient of the wing of the rotor/winged-body configuration at high speed flight.

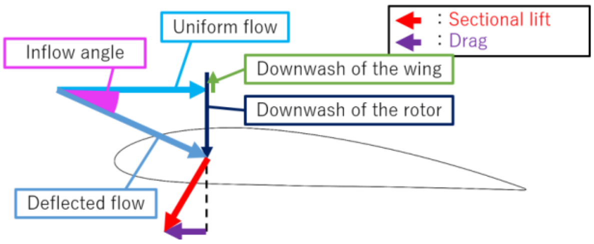

Fig. 12 The schematic of the aeromechanics which causes the increase of the drag coefficient of the wing of the rotor/winged-body configuration at low speed flight.

Fig. 13 shows the influence on the lift coefficient of the wing on the winged-body due to the rotor/winged-body aerodynamic interaction. This lift coefficient was obtained by extracting the lift coefficient of the wing section from the lift coefficient of the winged-body. This lift coefficient is nondimensionalized by dynamic pressure and the reference area of the winged-body. The lift coefficient decrement decreases as the advance ratio increases on both sides of the wing. The decrement of lift coefficient on the left side becomes closer to 0 as the advance ratio increases but that on the right side remains at a high advance ratio. The lift coefficient of both sides on the wing becomes closer to that on the isolated winged-body as the advance ratio increases. However, the influence on an aircraft has a different trend due to the increase in dynamic pressure, as shown Fig. 14. The change of lift of the wing was normalized by the total lift equal to the gross weight. Since the total lift is a constant value and independent of the advance ratio, the trend in Fig. 14 includes the effect of dynamic pressure. The lift of the left side becomes closer to the isolated winged-body as the advance ratio increases. However, the lift of the right side increases as the advance ratio increases. This trend of the right side in Fig. 14 means the following that the lift coefficient of the wing in Fig. 13 becomes closer to that on the isolated winged-body as the advance ratio increases, and it remains slightly different at high advance ratio, but the slight difference causes a significant influence that decreases the total lift by 5 % at an advance ratio of 0.7.

Fig. 15 shows the influence on the lift coefficient of the winged-body. The lift coefficient on the fuselage becomes closer to that on the isolated winged-body as the advance ratio increases. From Fig. 8, the decrease of the lift coefficient on the fuselage is caused by the decreasing of the velocity on the upper side of the nose of the fuselage. The decrement of the lift coefficient on the wing is significantly larger than that on the fuselage. The decrement of the lift coefficient of the winged-body is caused mainly by the right side of the wing, as shown Fig. 13 and 15.

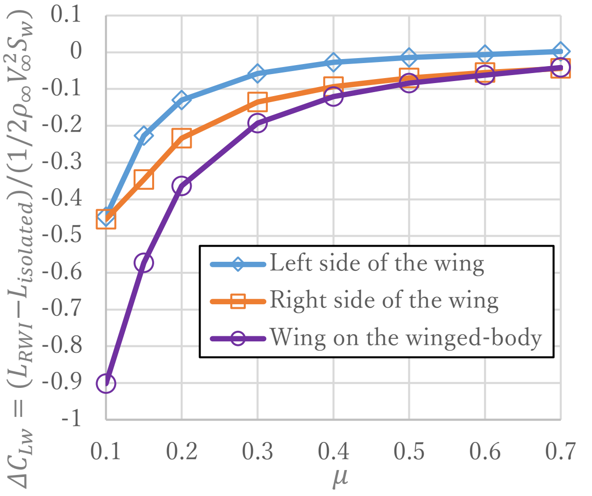

Fig. 13 The influence to the lift coefficient on the parts of the wing on the winged-body focusing on aerodynamic characteristics of the wing. (nondimensionalized by dynamic pressure and the reference area of the winged-body.)

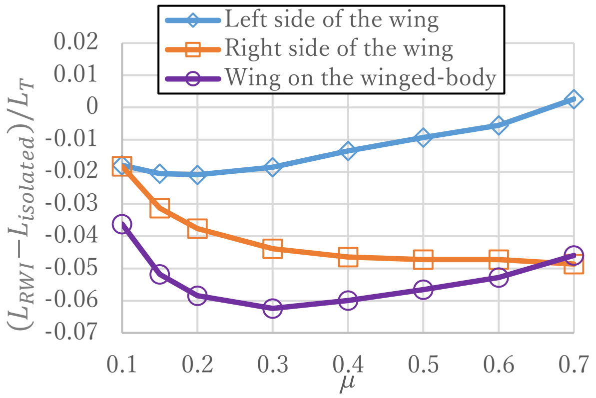

Fig. 14 The influence to the lift on the parts of the wing on the winged-body focusing on aerodynamic characteristics of an aircraft. (nondimensionalized by the total lift.)

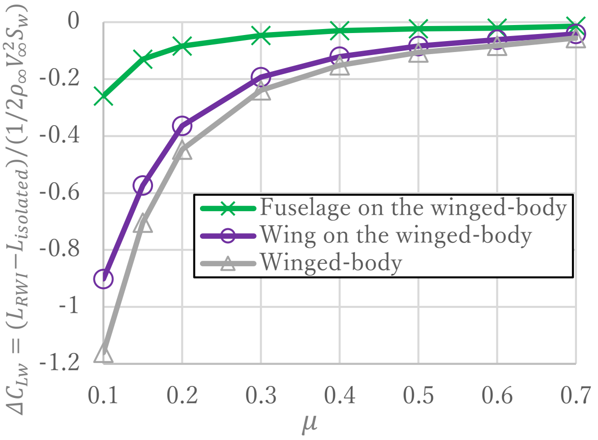

Fig. 15 The influence to the lift coefficient on the winged-body. (nondimensionalized by dynamic pressure and the reference area of the winged-body.)

Fig. 16 shows the influence on the drag coefficient of the wing on the winged-body due to the rotor/winged-body aerodynamic interaction. This drag coefficient was obtained by extracting the drag coefficient of the wing section from the drag coefficient of the winged-body. This drag coefficient is nondimensionalized by dynamic pressure and the reference area of the winged-body. The drag coefficient becomes negative or low at an advance ratio of 0.1 on both sides, and at an advance ratio 0.15 on the right side. At an advance ratio above 0.4, the increment of drag coefficient of the left side decreases as the advance ratio increases, but that of the right side does not decrease as rapidly as the left side of the wing while the advance ratio increases.

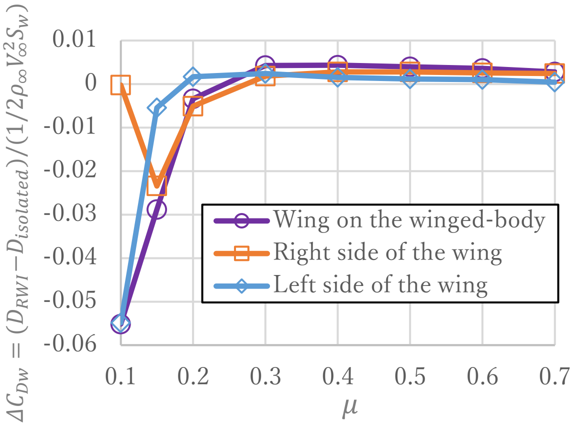

(a) Overall

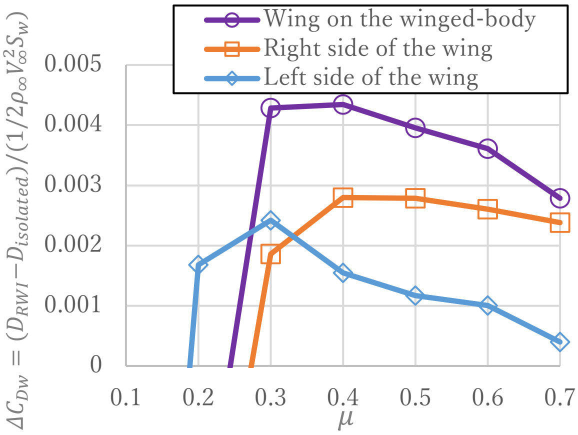

(b) Focus on high advance ratio

Fig. 16 The influence to the drag coefficient on the parts of the wing on the winged-body focusing on aerodynamic characteristics of the wing. (nondimensionalized by dynamic pressure and the reference area of the winged-body.)

The drag coefficient in Fig. 16 shows the aerodynamic characteristics of the wing, excluding the effect of dynamic pressure. Therefore the trend of increasing drag on an aircraft becomes different from the trend in Fig. 16. Fig. 17 shows the increment of drag normalized by the total lift to describe the influence on an aircraft. As in Fig. 14, since the total lift is a constant value and independent of the advance ratio, the trend in Fig. 17 includes the effect of dynamic pressure. The the right side's drag increases as the advance ratio increases from 0.3 to 0.7 but that of the left side does not increase as rapidly as the right side of the wing while the advance ratio increases. This trend in Fig. 17 is opposite of that in Fig. 16. Therefore, when considering an aerodynamic characteristic of a wing in a rotor/winged-body aerodynamic interaction, the effect of dynamic pressure should be noted, as in a fuselage in a rotor/fuselage aerodynamic interaction [15].

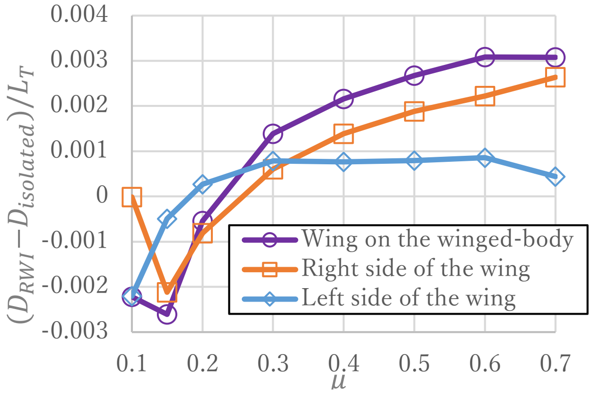

Fig. 17 The influence to the drag on the parts of the wing on the winged-body focusing on aerodynamic characteristics of an aircraft. (nondimensionalized by the total lift.)

Fig. 18 shows the increment of the drag coefficient of the winged-body. The increment of the drag coefficient of the fuselage is larger than that of the wing. The increment of the drag coefficient on the fuselage becomes positive for advance ratios from 0.1 to 0.7. From Fig. 8, the increasing of drag coefficient on the fuselage is caused by the decreasing of velocity on the upper side of the nose of fuselage. The nose of the fuselage is round, the upper surface on the nose has negative pressure if there is no rotor/winged-body aerodynamic interaction. However, the velocity on the upper side of the nose decreases compared to that of isolated winged-body due to the rotor downwash. Therefore, the drag coefficient on the fuselage increases in the rotor/winged-body aerodynamic interaction. The increment of the drag coefficient of the winged-body is caused mainly by the right side of the wing and the fuselage, as shown Fig. 16 and 18.

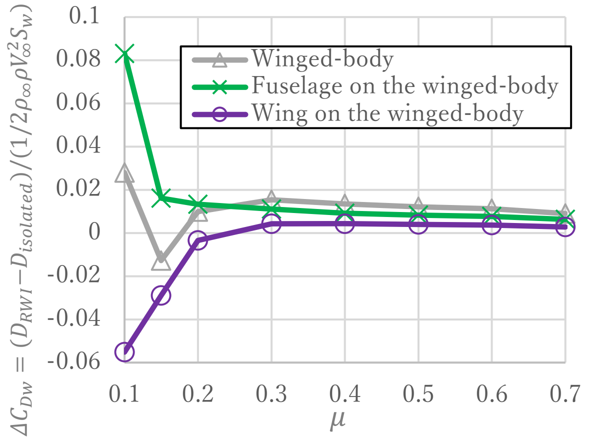

(a) Overall

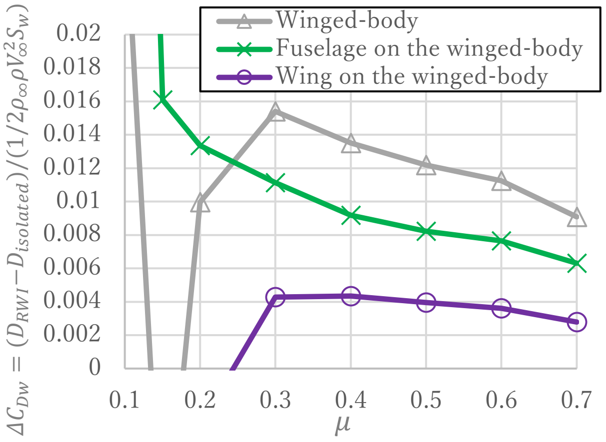

(b) Focus on high advance ratio

Fig. 18 The influence to the drag coefficient on the winged-body. (nondimensionalized by dynamic pressure and the reference area of the winged-body.)

Fig. 19 shows the lift-to-drag ratio of the wing on the winged-body. The data for the advance ratios of 0.1, 0.15 and 0.2 are deleted because the lift coefficient or/and the drag coefficient become negative. The lift-to-drag ratio of the left side becomes larger than that of the right side on the rotor/winged-body configuration. The lift-to-drag ratio of the wing on the rotor/winged-body configuration becomes closer to that on the isolated winged-body as the advance ratio increases.

Fig. 20 shows the lift-to-drag ratio of the winged-body. The lift-to-drag ratio of the winged-body on the rotor/winged-body configuration becomes closer to that of the isolated winged-body as the advance ratio increases.

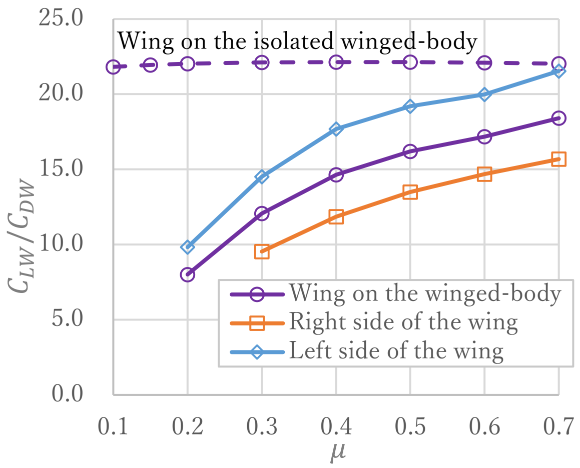

Fig. 19 The lift-to-drag ratio of the wing of the winged-body.

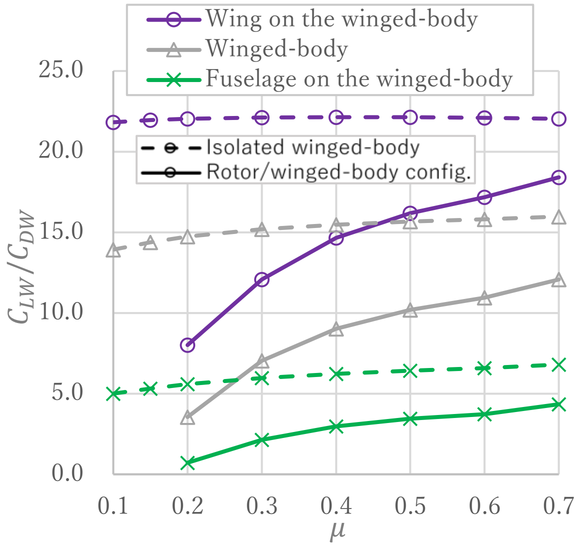

Fig. 20 The lift-to-drag ratio of the winged-body

6. Conclusion

The aerodynamic interaction between the rotor and the wing of a compound helicopter has been investigated through numerical simulations. The gross weight was constant, and the advance ratio changed from 0.1 to 0.7. The winged-body of the rotor/winged-body configuration in which this aerodynamic interaction occurs was compared to that of the isolated winged-body. This numerical simulation clarified the following:

1. The lift-to-drag ratio of both sides of the wing become closer to that of the wing of the isolated configuration as the advance ratio increases but

that of the right side, which is under the advancing side of the rotor, remains different to that of the isolated winged-body.

2. The lift and drag of the wing on winged-body were nondimensionalized by dynamic pressure and the reference area of the winged-body. This lift and drag coefficient of both sides on the wing of the rotor/winged-body configuration becomes closer to that of the isolated winged-body as the advance ratio increases, but that of the right side remains different to that of the isolated winged-body. However, the differences remaining in the lift and drag coefficient of right side has a significant impact on an aircraft at high advance ratios, resulting in high dynamic pressure.

3. The sectional drag coefficient on the left side becomes closer to that on the isolated winged-body, and that on the right side remains increased at the root at advance ratios from 0.3 to 0.7. At an advance ratio above 0.2, the sectional drag coefficient is larger on the left side and smaller on the right side than that on isolated winged-body. The negative sectional drag coefficient generates on left side at an advance ratio of 0.1 and on the right side at an advance ratio of 0.15.

4. The sectional lift coefficient of the wing on the rotor/winged-body becomes smaller than that on the isolated winged-body. The influence is stronger at the root than the tip on the wing, at the right side more than the left side and at low advance ratio than at high advance ratio. The negative sectional lift coefficient generates on both sides at an advance ratio of 0.1 and on the right side at an advance ratio of 0.15. The sectional lift coefficient on the left side becomes closer to that of the isolated winged-body as the advance ratio increases. The sectional lift coefficient on the right side remains different as the advance ratio increases.

Acknowledgment

We would like to thank Dr. Martin Wood (Kanazawa Institute of Technology) for his comments and editing on the early versions of this manuscript.

Reference

1. Ormiston, R. A. “Revitalizing Advanced Rotorcraft Research–and the Compound Helicopter: 35th AHS Alexander A. Nikolsky Honorary Lecture”, Journal of the American Helicopter Society, Vol. 61, No. 1,2016, pp. 1-23.
2. Walsh, D., Weiner, S., Arifian, K., Bagai, A., Lawrence, T., and Blackwell, R. “Development Testing of the Sikorsky X2 TechnologyTM Demonstrator”, 65th Annual Forum of the American Helicopter Society International, May 2009.
3. Blacha, M., Fink, A., Eglin, P., and Cabrit, P. “Clean Sky2: Exploring New Rotorcraft High Speed Configurations”, 43rd European Rotorcraft Forum, Sept. 2017.
4. Leishman, J. G. and Bi, N. “Experimental Investigation of Rotor/Lifting Surface Interactions”, Journal of Aircraft, Vol. 31, No. 4, 1994, pp. 846-854.
5. Sugawara, H., and Tanabe, Y. “Numerical Investigation of Rotor/Wing Aerodynamic Interactions at High Advance Ratios”, Journal of Aircraft, Vol. 56, No. 6, 2019, pp. 2285-2298.
6. Wentrup, M., Yin, J., Kunze, P., Streit, T., Wendisch, J., Schwarz, T., Pinacho, J., Kicker, K., and Fukari, R. “An Overview of DLR Compound Rotorcraft Aerodynamics and Aeroacoustics Activities within the CleanSky2 NACOR Project”, American Helicopter Society 74th Annual Forum, May 2018.
7. Frey, F., Thiemeier, J., Öhrle, C., Keßler, M., and Kr¨amer, E., “Aerodynamic Interactions on Airbus Helicopters’ Compound Helicopter RACER in Cruise Flight”, the VFS International 76th Annual Forum &Technology Display, Oct. 2020.
8. Sugawara H., Tanabe Y., and Kameda, M. “Effect of Lift-Share Ratio on Aerodynamic Performance of Winged Compound Helicopter”, Journal of Aircraft, Vol. 58, No. 5, 2021, pp. 997-1009.
9. Hamamoto, Y., Akasaka, T., Tanabe, Y., and Sugawara, H., “Aerodynamic Interaction Between a Rotor and a Wing on Compound Helicopter in Forward Flights”, 53rd Fluid Dynamics Conference / 39th Aerospace Numerical Simulation Symposium, Jun. 2021. (in Japanese)

10. Tanabe, Y., Sugawara, H., Kobiki, N., Kobayashi, W., Hayashi, H., and Satou, R. “Experimental and Numerical Investigation of Interaction Between Rotor and Wing at High Advance Ratio”, Vertical Flight Society 76th Annual Forum, Oct. 2020.
11. Davis, S. J. “Predesign Study for a Modern 4-Bleaded Rotor for RSRA”, NASA Contractor Report, 166155, 1981.
12. Bousman, W. G. “Aerodynamic Characteristics of SC1095 and SC1094 R8 Airfoils”, NASA /T2003-212265, AFDD/TR-04-003, Dec. 2003.
13. Tanabe, Y., Saito, S. and Sugawara, H. “Construction and validation of an Analysis Tool Chain for Rotorcraft Active Noise Reduction”, 38th European Rotorcraft Forum, Sept. 2012.
14. Prouty, R. W. “Helicopter Performance, Stability, and Control”, Krieger Publishing Company, Malabar, Florida, 2005, pp. 698.
15. Leishman, J. G., “Principles of Helicopter Aerodynamics”, 2nd ed., Cambridge Univ. Press, Cambridge, England, U.K., 2006, pp. 663.